catalysts

MDPI

Article

How Effective Is Graphitization of Biomasses for the Carbon Stability of Pt/C ORR Catalysts?

Henrike Schmies [1,*,†], Nina Bengen [1,†], Julia Müller-Hülstede [1], Olayinka Ahmed Ibitowa [2], Peter Wagner [1] and Michael Wark [2]

[1] German Aerospace Center, Institute of Engineering Thermodynamics, 26129 Oldenburg, Germany
[2] Institute of Chemistry, Carl von Ossietzky University Oldenburg, 26129 Oldenburg, Germany
* Correspondence: henrike.schmies@dlr.de
† These authors contributed equally to this work.

Abstract: Catalysts for the oxygen reduction reaction (ORR) in PEM fuel cells are commonly constituted of Pt-based nanoparticles and a carbon support originating from fossil resources. In order to employ a more sustainable carbon support, activated sawdust was chosen in this study. This was firstly steam-activated at 750 °C and then thermally treated at elevated temperatures up to 2800 °C and reducing conditions at 1100 °C. Various physical characterization methods were applied to systematically relate treatment parameters to surface and structural properties of the carbon material. Deposition of small Pt nanoparticles on the biochar-based supports yielded in ORR active catalysts which were analyzed by thin-film rotating disc electrode measurements. The activity and stability towards the ORR of these novel catalysts was compared to a commercial raw oil-based Pt/C and the influence of support modification on the ORR performance was discussed.

Keywords: biomass; carbon support; PEMFC; ORR; stability; sawdust; activated biomass; platinum catalyst; thermal treatment; graphitization

Citation: Schmies, H.; Bengen, N.; Müller-Hülstede, J.; Ibitowa, O.A.; Wagner, P.; Wark, M. How Effective Is Graphitization of Biomasses for the Carbon Stability of Pt/C ORR Catalysts?. *Catalysts* **2023**, *13*, 343. https://doi.org/10.3390/catal13020343

Academic Editor: Ermete Antolini

Received: 19 December 2022
Revised: 13 January 2023
Accepted: 1 February 2023
Published: 3 February 2023

1. Introduction

In order to achieve the goals of the Paris Climate Agreement, namely decreasing the impact of global warming [1], the switch to CO_2 neutral energy sources such as solar or wind power is unavoidable. Electrical energy generated from such sources can be used to split water by means of electrolysis, producing green hydrogen [2]. This hydrogen can be applied in fuel cells for power recovery or in vehicles [3]. One of the most established fuel cell type is the proton exchange membrane fuel cells (PEMFCs) [4]. In PEMFCs, water and electrical energy are produced by the reduction of oxygen at the cathode and the oxidation of hydrogen at the anode [5]. PEMFCs can be divided into low temperature (LT-PEMFC, 60–90 °C) and high temperature (HT-PEMFC, 120–200 °C) systems. The cell components are each adapted to the operating conditions of the two types [4].

One of the main components of the PEMFC is the membrane electrode assembly (MEA). In general, the membrane and catalysts of anode and cathode are majorly determining the efficiency and lifetime of the fuel cell [6]. Especially an optimized catalyst at the cathode side, where the oxygen reduction reaction (ORR) takes place, can strongly contribute to the performance by lowering the reactions overpotential. The catalyst usually consists of platinum nanoparticles on a porous and graphitic carbon support. Commercially available catalysts contain expensive and crude oil-based carbon blacks, such as Ketjenblack® EC-600JD or Vulcan® XC-72 as Pt support [7]. For use as PEMFC catalyst, (i) high ORR activity, (ii) electrical conductivity, (iii) electrochemical stability, (iv) chemical stability, (v) specific and porous surface area with small particle size and (vi) strong linkage between platinum nanoparticle and support material are desired [8]. During fuel cell operation, different degradation paths of the catalyst occur which result in a decrease in

performance. Degradation mechanisms such as platinum dissolution, detachment and agglomeration are known for the catalyst itself [9]. Furthermore, carbon corrosion of the support is well known to contribute to activity loss of the Pt catalyst. All degradation processes take place partly simultaneously or can be interconnected [10]. Corrosion of the carbon support is triggered by harsh conditions, such as elevated temperature, low pH and high potentials present in PEMFCs [11,12]. Carbon corrosion becomes significant at potentials above 1.1 V_{RHE} (present during FC start/stop processes) and can furthermore be catalyzed by Pt [13]. It can lead to a partial or complete loss of the structural integrity of the catalyst/support couple and to a weakening of the platinum carbon bonding [14].

To minimize the occurrence of carbon corrosion an optimization of the carbon support towards higher stability is necessary. This can be achieved by adjusting and optimizing morphological and structural properties such as graphitic fraction, pore volume and size [15]. Modification or doping of the support with heteroatoms represents another option for preventing or minimizing carbon corrosion [16–18]. Moreover, from a more sustainable approach, activated biomasses have already shown to be a suitable carbon support [19].

Literature examples show the utilization of biomasses as carbon support with a defined pore structure and a high surface area up to 1000 $m^2\ g^{-1}$ achieved by activation procedures. Dhelipan et al. applied phosphoric acid activated orange peels as Pt support and investigated the ORR activity in acidic environment. They explained a low electrochemical active surface area determined by hydrogen underpotential deposition ($ECSA_{HUPD}$) with a large pore diameter of the carbon material, resulting in trapped and electrochemically inactive platinum particles [20]. The same group utilized mushroom compost as mesoporous carbon support by heat treatment of the raw material at 800 °C. They found superior electrochemical stability after 10,000 potential cycles from 1.0 to 1.6 V_{RHE} compared to a standard mesoporous carbon catalyst [21]. In our previous study, we used hydrothermally treated coconut shells and compared chemical KOH- and physical vapor activation as well as thermal activation at 1100 °C. Due to its physical properties, the activated biochar from pyrolysis was the most suitable carbon support in terms of specific surface area, mesopore fraction and electrical conductivity. We revealed that a higher temperature for pyrolysis would beneficial for an increase in stability [22]. Overall, it can be concluded that biomass-based carbons represent a promising class of support materials. However, improvements in terms of electrochemical parameters and overall stability must be made.

In this study, the influence of the treatment temperature of activated sawdust on its structural properties is investigated. The aim is to obtain a graphitic carbon support and explore the impact on the electrochemical stability. For this purpose, waste-biomass in terms of sawdust was steam-activated and then thermally treated at temperatures of 1500, 1800, 2100 and 2800 °C under an inert gas atmosphere. Furthermore, the influence of reducing conditions by a hydrogen content of 50 vol.% at 1100 °C was investigated. The novel sustainable activated biomasses underwent intense physical characterization and were used as carbon supports for 40 wt.% platinum catalysts. The ORR activity and stability were determined and compared to a commercial Pt/C reference catalyst by rotating disk electrode (RDE) studies. This allowed conclusions to be drawn about the influence of graphitization for biomass-based ORR catalysts in PEMFC.

2. Results and Discussion

The approach for obtaining a Pt-based catalyst with a support which is made from modified activated sawdust is schematically shown in Figure 1. As starting material, the raw sawdust (SD) was taken and then treated at 750 °C in a steam activation step to receive the activated sawdust (aSD). Afterwards, a thermal treatment at different elevated temperatures (T) up to 2800 °C is applied to receive (partly) graphitized carbons (gaSD_*T*). Additionally, the influence of a reducing atmosphere from treatment in 50 vol.% H_2 is analyzed. The received modified and activated carbons are then used as support for Pt nanoparticles (Pt/gaSD_*T*). The previous materials were extensively physically and electrochemically characterized and the results are described and discussed in the following paragraphs.

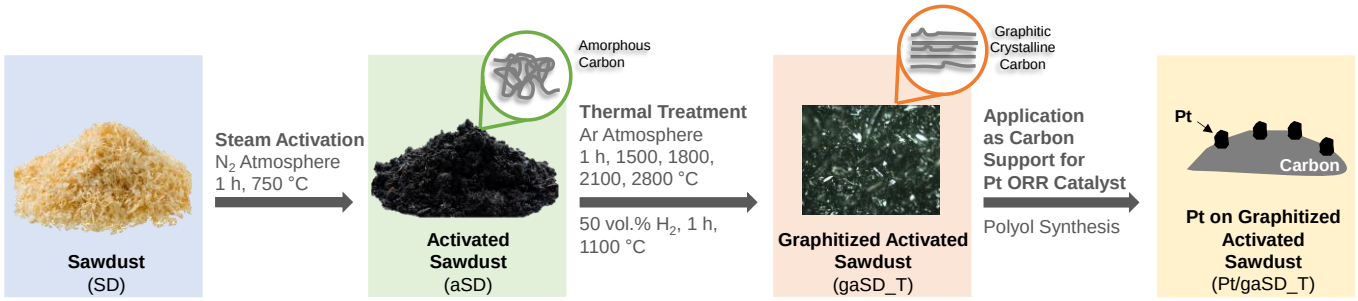

Figure 1. Schematic overview of the treatment of sawdust, the change in carbon structure and its use as a platinum ORR catalyst.

2.1. Physical Characterization of Thermally Modified Sawdust

The porosity of the activated and modified sawdust was accessed by nitrogen sorption experiments. All isotherms are shown in Figure 2a and proceed according to type IV with a hysteresis of type H2 of the IUPAC classification [23,24]. The isotherms exhibit a hysteresis, which occurs in multilayer physisorption due to capillary condensation in mesopores. Furthermore, the type IV isotherms induce an undefined distribution of pore shape and size [23,24]. The aSD as starting material reveals a comparatively high specific surface area of 711 m^2 g^{-1} and a pore volume of 0.707 cm^3 g^{-1} comprising around 18% (0.123 cm^3 g^{-1}) micropores (Figure 2b).

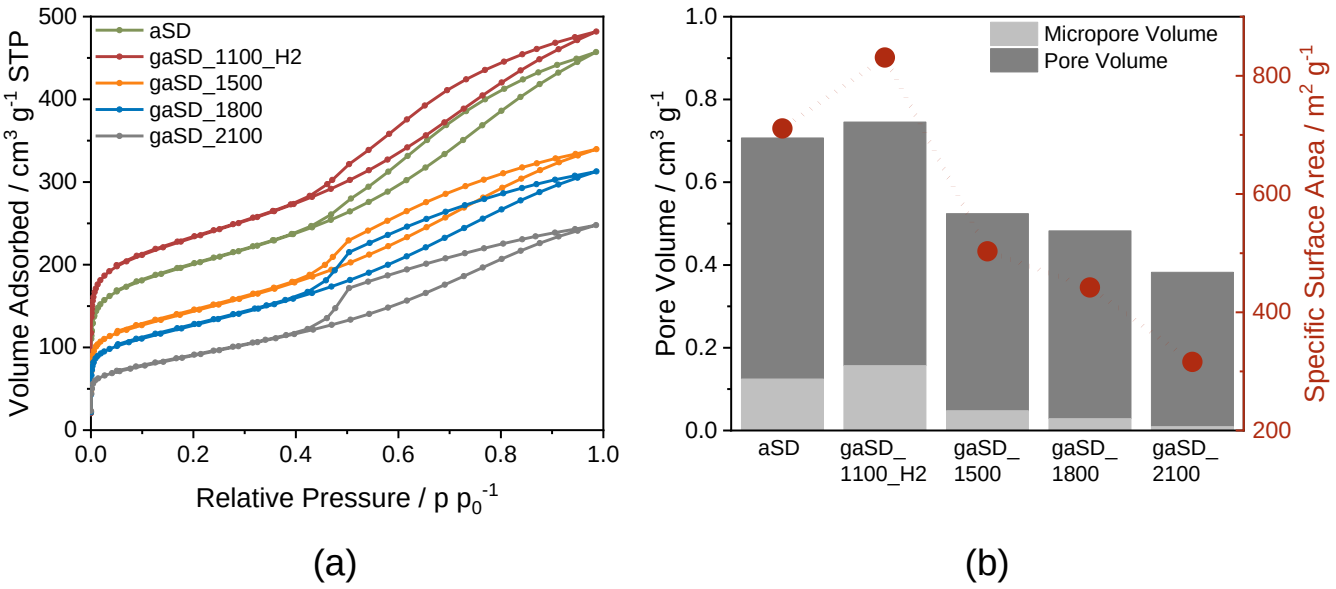

Figure 2. (**a**) Nitrogen sorption isotherms and (**b**) specific surface area and micro−/pore volume of untreated and thermally treated activated sawdust.

Thermal treatment of aSD at 1100 °C under reducing conditions (gaSD_1100_H2) leads to an increase in specific surface area of 14% (711 to 831 m^2 g^{-1}) and increased pore volume of 0.745 cm^3 g^{-1}. This is mainly related to a higher micropore volume (0.123 to 0.157 cm^3 g^{-1}). The aSD might still contain a large number of inorganic compounds after steam activation, which are likely to block pores. Such compounds could be removed by the reducing conditions making the pores accessible and leading to a higher BET surface area [25]. Due to the increasing thermal treatment temperature for the aSD, the pore volume and the specific surface area decrease (Figure 2b). For example, gaSD_2100 possesses a BET surface area of 316 m^2 g^{-1} and a pore volume of 0.382 cm^3 g^{-1} of which only around 2% is micropore volume; i.e., most of the pore volume relates to mesopores. Compared to aSD, the BET surface area of gaSD_2100 decreased by 56% and the micropore volume

decreased by 93% due to thermal treatment. It can be assumed that the micropore walls are unstable and mesopores form by the fusion of micropores, causing the physical surface area to reduce. On the other hand, the specific surface area may also decrease due to the local formation of graphitic structures and crystallites in the biochar matrix [26,27].

To evaluate the graphitic character and the crystallinity of the sawdust-based carbon materials treated at different temperatures, powder X-ray diffraction (PXRD) and Raman spectroscopy were applied. The PXRD patterns of the analyzed materials are plotted in Figure 3a together with the reference graphite pattern. Here, it can be observed that with increasing treatment temperature a broad peak at around 25° of 2θ evolves. Aliphatic side chains and heterocycles lead to disorder in the structure, which results in a broadening of the (002)-reflex at 26° [28]. In addition, it can be assumed that other carbon structures such as amorphous and turbostratic phases are present besides graphitic carbon which cause a broadening of the reflex [29]. For the carbons graphitized at 2100 °C and higher, a sharp peak around 26° 2θ becomes visible (Figure 3b) which can be assigned to the (002) planes of graphite. In case of gaSD_2800 the whole reflex becomes narrower and more intense. Therefore, it can be assumed that from a thermal treatment of aSD between 1800 and 2100 °C, a crystalline structure with graphitic character is formed. By analyzing the layer distance d(002) as shown in Figure 3b, it becomes visible that the layer distance approaches that of reference graphite (3.40 Å) with increasing treatment temperature. The diffractograms of aSD and gaSD_1100_H2 cannot be matched with the graphite reference pattern. Instead, here the peaks are most presumably originating from inorganic crystalline residues that remain in the biochar after activation and are furthermore not removed or transformed under reducing conditions in the case of gaSD_1100_H2. However, after thermal treatment at 1500 °C or higher, these crystalline compounds are not present anymore.

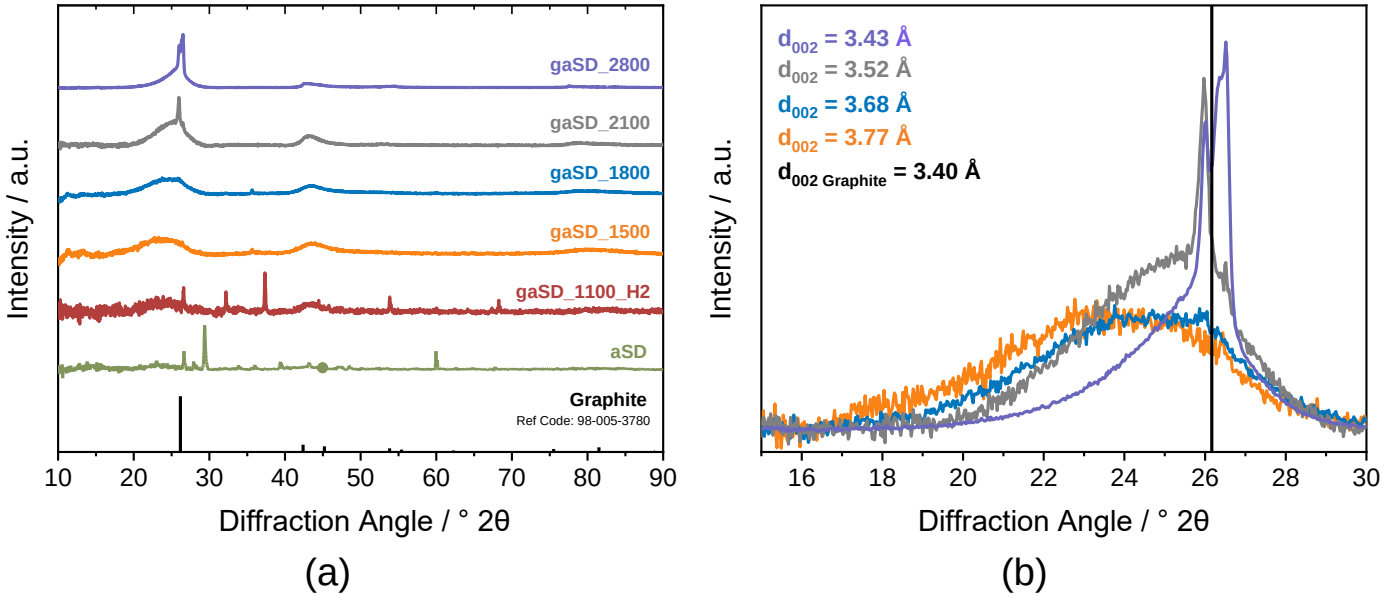

Figure 3. (**a**) PXRD patterns of six different carbons and graphite reference pattern from database (reference code: 98-005-3780) [30]; (**b**) zoom of diffractogram from 15° to 30°.

Results of Raman spectroscopy including the spectra and fitting (exemplarily shown for sample gaSD_2100) are presented in Figure 4. The Raman spectra (Figure 4a) in the range of 500–3500 cm^{-1} are plotted and the characteristic D1 (defect)- and G (graphitic)-bands around 1350 cm^{-1} and ~1580 cm^{-1} for carbon materials in the first-order spectra have been marked. The G-band is formed by the vibration of sp^2 structures. If a disordered structure is existing in the sp^2/sp^3 hybridized carbon structure, this becomes evident in the resonance spectrum by the D-band. For carbon materials containing a high proportion of amorphous carbon, peaks only in the first-order spectrum can be found. There, the D1 and

G bands are not baseline-separated induced by the appearance of a D3 band, so that the fitting is necessary to determine the ratio of these compounds. Furthermore, the D1- und G-bands are composed of five bands which can be deconvoluted by a fitting approach. The D1-, D2- and D4-bands are originating from non-ordered graphitic planes, whereas the D3-band is generated by amorphous carbon structures and functional groups as well as heteroatoms [31,32]. Graphitic carbons are characterized by a second-order spectrum additional to the first-order spectrum (Figure 4c) and are described as overtone of the first-order spectrum. In this region the G'-band at 2650 cm^{-1}, the D+G-band (~2950 cm^{-1}) and the 2D'-band (~3230 cm^{-1}) can be observed. Additionally, a 2G-band between the D+G- and 2D'-band can be formed.

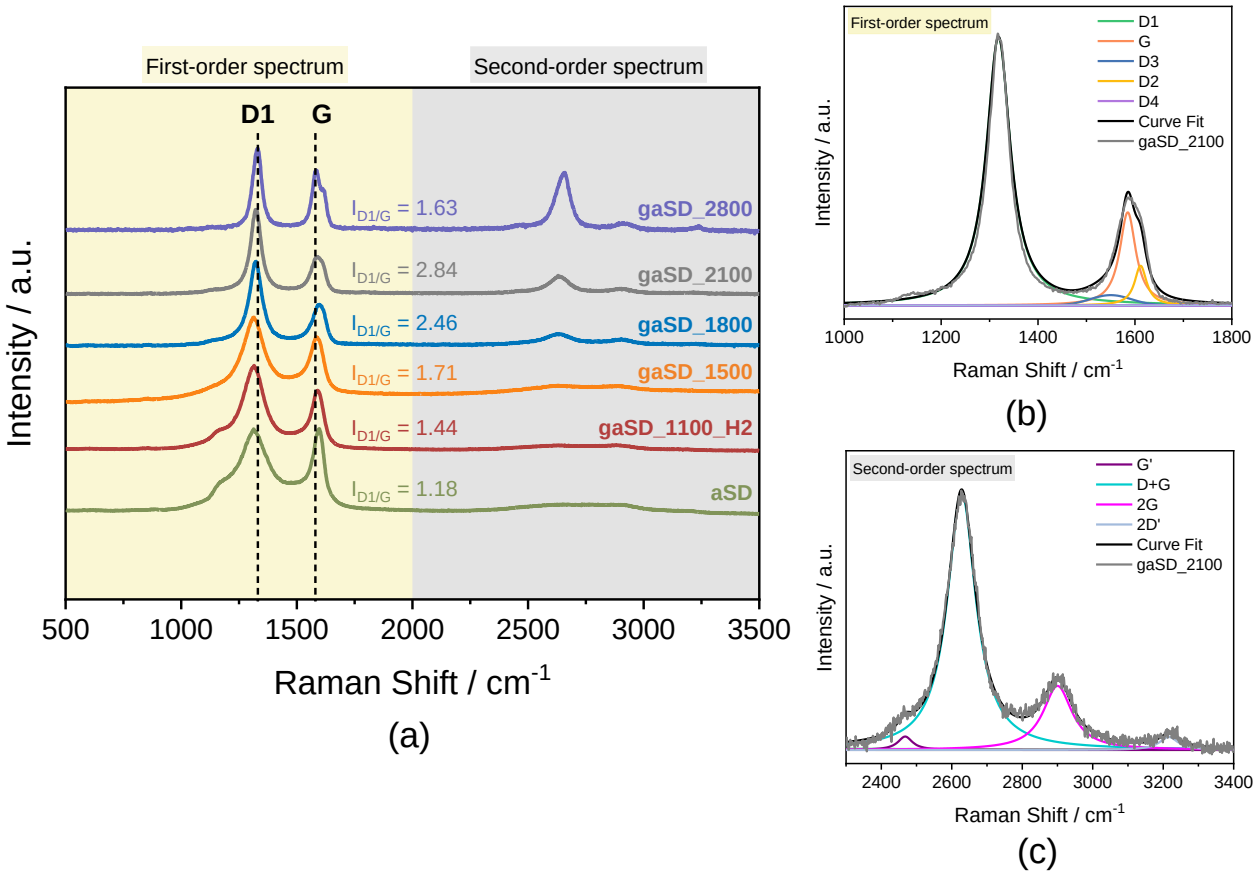

Figure 4. (**a**) Raman spectra of untreated and modified aSD; (**b**) example of curve fitting of first-order Raman spectra and (**c**) example of curve fitting of second−order Raman spectra. Fitting parameters based on literature [33–37].

Figure 4a shows that a treatment at higher temperature leads to an increasingly stronger formation of the second-order spectrum. As already mentioned, this is an indication of increasing graphitic character. A high intensity ratio of the D1- to G-band in the first-order spectrum indicates a graphitic character of carbon. In case of graphitization of an amorphous material, such as sawdust in this study, the ratio may be assumed to increase with increasing graphitic character [37]. Figure 4a shows that with increasing treatment temperature the intensity ratio $I_{D1/G}$ increases. This trend is in line with the literature and suggests that the graphitic degree increases with increasing treatment temperature of the aSD [37]. However, this trend is opposite between 2100 and 2800 °C, here the higher treatment temperature leads to a decrease in intensity ratio of D1 to G ($I_{D1/G}$). According to FERRARI AND ROBERTSON, for a graphitic starting material, the decrease of $I_{D1/G}$ indicates a higher order [37]. Furthermore, the $I_{D1/G}$ ratio of graphitic materials (L_a < 2 nm) depends

on the cluster diameter/plane length L_a and the atomic distance C as described in the TUINSTRA AND KOENIG (TK)-equation [37]:

$$\frac{I_{D1}}{I_G} = \frac{C}{L_a} \quad (1)$$

whereas for smaller crystallites and thus lower graphitic character, the TK-Equation (1) is invalid. There, the $I_{D1/G}$ value increases with increasing crystallite size. Based on the relationship between the $I_{D1/G}$ value and the crystallite size according to Equation (1), the SCHERRER Equation (3) was used to determine the crystallite size from the PXRD patterns in Figure 3a. This resulted in a crystallite size of 19 Å for gaSD_2100, whereas the crystallite size of gaSD_2800 was found to be 204 Å. Since the crystallite size of gaSD_2800 is above 2 nm (20 Å), it can be assumed that based on the TK-Equation (1), the $I_{D1/G}$ decreases due to the lager crystallites. With 19 Å, the value of gaSD_2100 is still just below this limit [37,38].

2.2. Characterization of Platinum Catalysts

The above-described carbons were used as support for Pt catalysts. Therefore, small Pt nanoparticles were synthesized in a polyol process [39] and afterwards deposited on the carbon. A nominal weight loading of Pt on the carbon support of 40 wt.% was chosen for this study. A commercial 40 wt.% Pt/C (TEC10E40E by TANAKA) with a raw-oil based high surface area carbon (HSAC) support was taken as reference catalyst.

Catalyst Morphology and Metal Loading

To analyze the catalysts morphology and the Pt particle distribution as well as its size on the different supports, transmission electron microscopy (TEM) was applied. Figure 5 shows TEM images of all six samples as well as the reference catalyst. First, it can be observed that all self-prepared catalysts except Pt/gaSD_2800 reveal a relatively comparable morphology (Figure 5a–e). The carbon support seems not to have a defined structure with repeating units. The distribution of the small Pt nanoparticles is relatively homogeneous, thick material aggregates block the view on the sample in some parts. The catalyst Pt/gaSD_2800 exhibits a sheet-like carbon morphology with Pt agglomerates in some regions (Figure 5g). For the reference catalyst Pt/C Ref in Figure 5h, the support consists of spherical carbon particles typical for a high surface area mesoporous carbon [40]. Moreover, the small Pt nanoparticles are homogeneously distributed on the support with agglomerates in some parts.

The average Pt nanoparticle diameters are listed in Table 1 and were received by measuring at least 300 particles per sample. All samples despite Pt/gaSD_2800 reveal comparable average Pt diameters in the range of 1.0–1.70 nm. Most likely due to the observed agglomeration from TEM images, the obtained particle size of Pt/gaSD_2800 is larger and displays a higher standard deviation. However, as the nanoparticles are formed during the polyol process which was the same for all catalysts, the agglomeration must have happened afterwards during the deposition and is therefore correlated to the carbon surface properties. For Pt/gaSD_2800, the high degree of graphitization and most likely changed surface properties are probably the cause for the observed carbon morphology and agglomeration of the Pt nanoparticles.

The Pt weight loading on the carbon support was determined by inductively coupled plasma mass spectrometry (ICP-MS) quantitative analysis and the results are listed in Table 1. The target loading of 40 wt.% was achieved for the catalysts Pt/aSD and Pt/gaSD_1100_H2, while for all other catalysts, a lower value in the range of 28.1–36.5 wt.% was obtained. This might most likely be due to different surface properties and loss of surface functional groups after thermal treatment at temperatures of 1500 °C and above. Consequently, the attachment of the nanoparticles on the carbon surface is not strong enough so that Pt nanoparticles are washed out during the cleaning step. An insufficient Pt attachment on highly graphitized support was also observed in literature if no surface functionalization was implemented [41,42]. For the commercial catalyst a Pt loading of around

32 wt.% was measured by ICP-MS. Furthermore, we verified this value by thermogravimetric analysis (TGA) and could confirm this value (see Figure S2 in the Supplementary Material). This metal content is lower than the indicated loading of 40 wt.% and might be due to manufacturing batch differences.

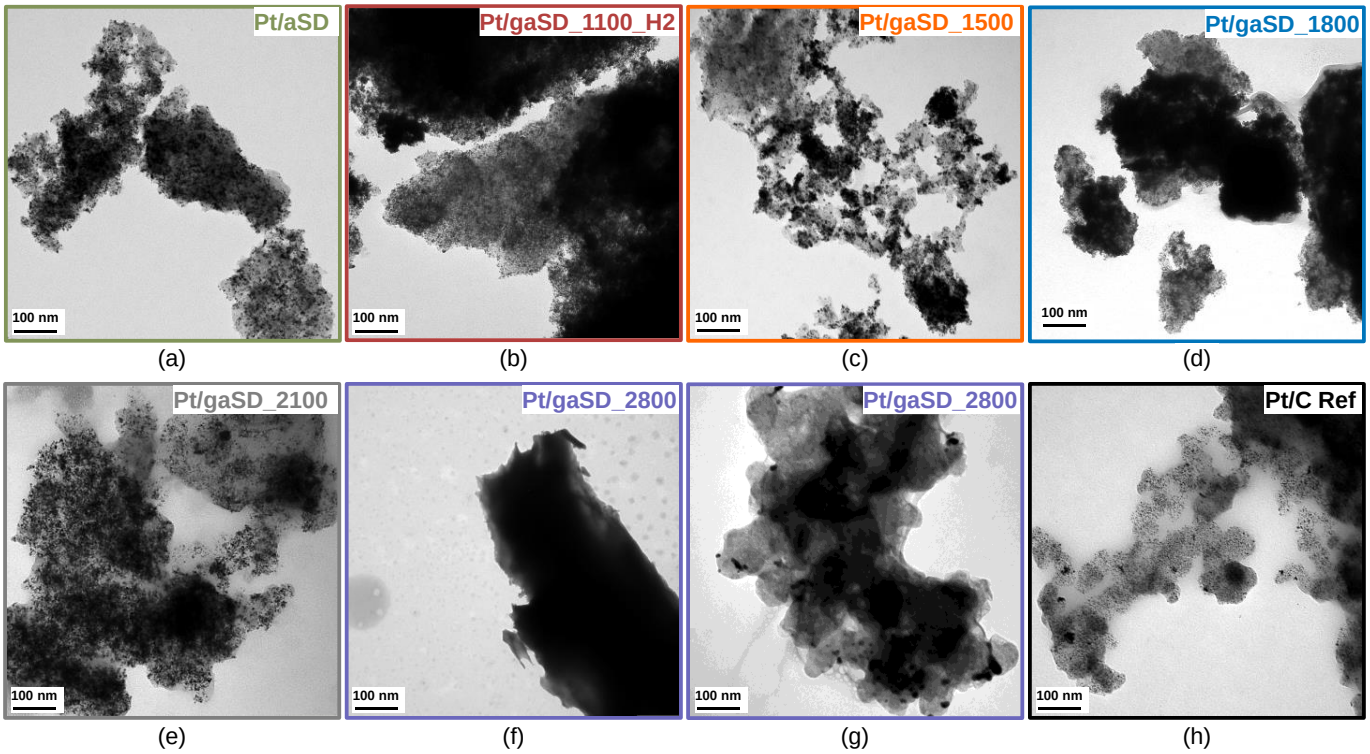

Figure 5. Transmission electron micrographs of Pt catalysts: Pt/aSD (**a**), Pt/gaSD_1100_H2 (**b**), Pt/gaSD_1500 (**c**), Pt/gaSD_1800 (**d**), Pt/gaSD_2100 (**e**), Pt/gaSD_2800 (**f**,**g**) and Pt/C ref (**h**).

Table 1. Nanoparticle diameter and platinum content of catalysts, obtained from TEM images and ICP-MS measurements.

	Nanoparticle Diameter/nm	Pt Content $_{ICP-MS}$/wt.%
Pt/aSD	1.70 ± 0.72	39.3
Pt/gaSD_1100_H2	1.48 ± 0.54	41.6
Pt/gaSD_1500	1.03 ± 0.36	28.1
Pt/gaSD_1800	1.09 ± 0.25	29.1
Pt/gaSD_2100	1.51 ± 0.51	31.3
Pt/gaSD_2800	3.14 ± 1.17	36.5
Pt/C ref	1.15 ± 0.59	31.8

2.3. Electrochemical Characterization

Four catalysts were chosen for electrochemical characterization to evaluate the activity and stability towards ORR in acidic electrolyte. This includes the catalyst based on the aSD as an internal reference and Pt/C ref as state-of-art commercial reference. Furthermore, the aSD treated under reducing conditions at 1100 °C which shows the highest Pt content and the catalyst with the highest graphitized character and comparable particle size from TEM (Pt/gaSD_2100) were chosen. In case of Pt/gaSD_2800, it was not possible to disperse the sample in the ink due to rough material aggregates, which are most likely due to the high degree of graphitization of the carbon.

ORR curves from the initial characterization are shown in Figure 6a. Here, it can be seen that the highest activity is achieved for the reference catalyst, followed by Pt/gaSD_1100_H2 and comparable low activities for Pt/aSD and Pt/gaSD_2100. Furthermore, the self-

prepared catalysts are not reaching the limiting current density region of the Pt/C ref as the active sites of the biochar catalysts might be blocked for O_2 diffusion by large catalyst aggregates. Possible reasons for that might be an inhomogeneous thin film on the RDE due to different carbon properties of the treated biochars.

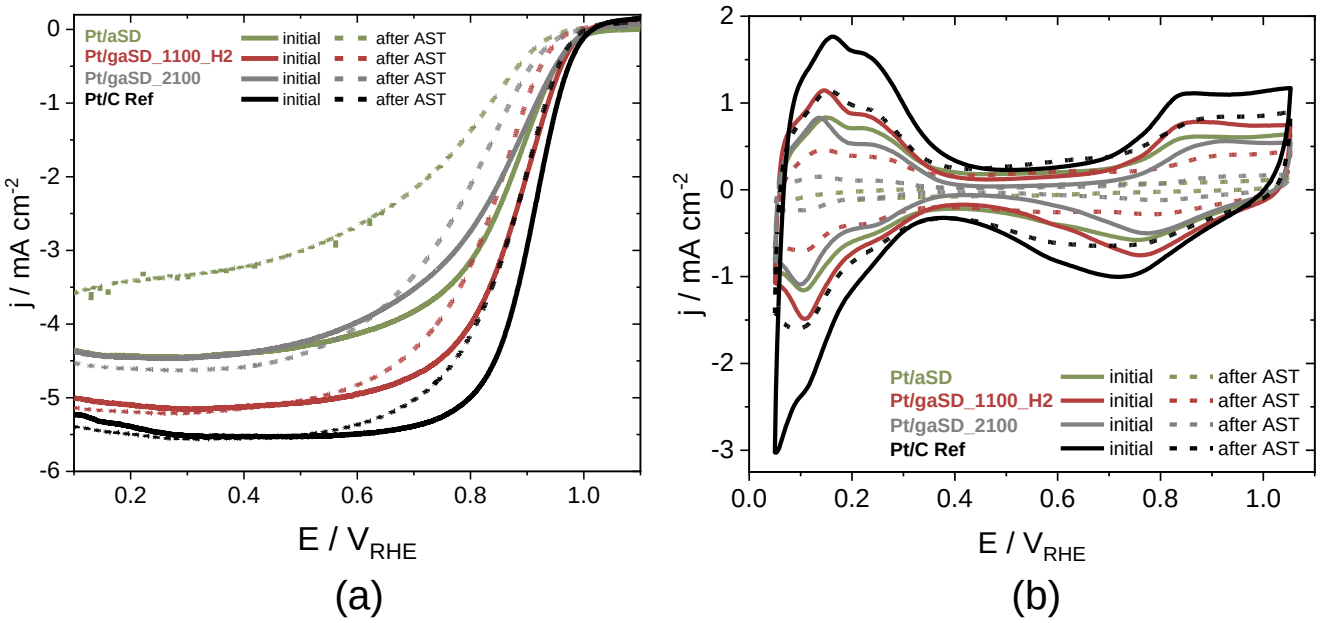

Figure 6. Electrochemical characterization of Pt/aSD, Pt/gaSD_1100_H2, Pt/gaSD_2100 and Pt/C ref before and after the AST (0.6–1.5 V_{RHE}, 5000 cycles) as (**a**) ORR activity curves in O_2−saturated 0.1 M $HClO_4$ electrolyte and 1600 rpm and (**b**) CVs in N_2-saturated electrolyte. Catalyst loading was 40 μg_{Pt} cm^{-2}.

The corresponding mass activities, determined at 0.9 V_{RHE} are shown in Figure 7. The catalysts based on aSD reveal activities in the range of 57–83 A g_{Pt}^{-1} which is obviously lower than that of Pt/C ref with 188 A g_{Pt}^{-1}. This activity is comparable with results found in literature for similar commercial Pt/C catalysts based on high surface area carbons [43]. It is furthermore observed that Pt/gaSD_1100_H2 shows an improved activity compared to Pt/aSD and Pt/gaSD_2100 (see Figure 7).

It is worth mentioning that a highly graphitized support in case of Pt/gaSD_2100 does not improve the catalytic properties compared to the catalyst with the untreated aSD. However, the support treated in hydrogen atmosphere improves the activity of the catalyst to some extent.

The CVs of all four catalyst are plotted in Figure 6b showing the hydrogen underpotential deposition (HUPD) region (0.05–0.40 V_{RHE}) as well as the Pt-O/OH region at higher potentials. In comparison of the four catalysts, again the Pt reference shows the highest currents resulting in an $ECSA_{HUPD}$ of 81 m^2 g_{Pt}^{-1} (see also Figure 7), which is line with literature results [43]. The lowest $ECSA_{HUPD}$ is found for Pt/aSD with a value of 26 m^2 g_{Pt}^{-1} while the determined $ECSA_{HUPD}$ for Pt/gaSD_1100_H2 and Pt/gaSD_2100 are in the intermediate range and very comparable with 43 and 44 m^2 g_{Pt}^{-1}. Generally, these values would be insufficient for fuel cell application, as high ECSA values of 60 m^2 g_{Pt}^{-1} and above are desired [44]. The observed trend of ECSA supports the before mentioned assumption that the accessibility of Pt active sites on the biochars is lower compared to the Pt/C ref. A particle size effect can be excluded, as the nanoparticle sizes determined from TEM analysis were all in the same range (see Table 1). By looking at the double layer capacity of the catalysts based on aSD in the CV at around 0.4–0.5 V_{RHE} it can be seen that the highest capacity is observed for the support with the largest surface area from BET analysis (Figure 2) and vice versa.

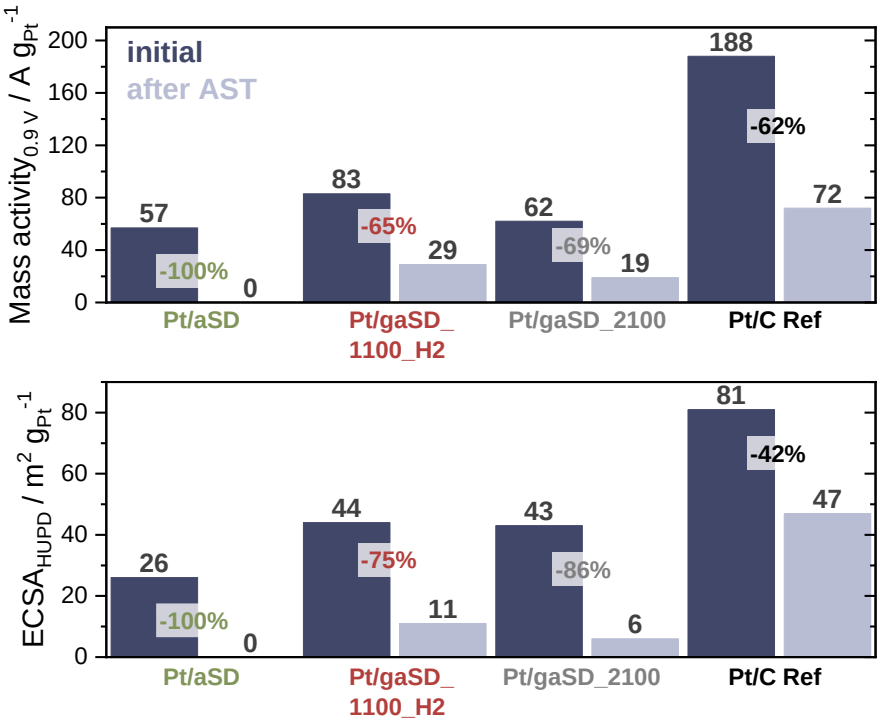

Figure 7. Mass activities at 0.9 V_{RHE} and $ECSA_{HUPD}$ for catalysts Pt/aSD, Pt/gaSD_1100_H2, Pt/gaSD_2100 and Pt/C ref before (initial) and after the AST (0.6−1.5 V_{RHE}, 5000 cycles). Averaged values of two electrochemical measurements are shown, for single values please check Figure S1 in the Supplementary Material.

After the initial characterization, an accelerated stress test (AST) in the range of 0.6–1.5 V_{RHE} for 5000 cycles was performed. An AST under these harsh conditions was chosen to provoke Pt catalyst degradation as well as carbon corrosion and includes a fuel cell operating range (below 1 V_{RHE}) and start/stop conditions (above 1 V_{RHE}). The ORR curves and the CVs after the AST are shown in Figure 6 and the resulting values for mass activities and $ECSA_{HUPD}$ are presented in Figure 7. Here, it can be noticed that Pt/aSD loses its initial activity and $ECSA_{HUPD}$ completely. The ORR curve shows some activities left; however, the CVs only show very little currents without any peaks (Figure 6). This leads to the assumption that all ORR active Pt nanoparticles have been degraded during the AST. In case of Pt/gaSD_1100_H2 and Pt/gaSD_2100 activity losses of 65% and 69%, respectively, are observed (Figure 7) which is very comparable to the Pt/C ref. As currents in the limiting current density region and double layer capacity in CV do not severely change after the AST for both catalysts, it is most likely that active catalyst material is not deactivated or detached triggered by carbon corrosion. Instead, growth, agglomeration and dissolution of Pt particles leads to a reduced ORR activity. This is not the case for Pt/aSD, where obviously carbon corrosion is dominating the degradation. $ECSA_{HUPD}$ decreases to a comparable extent around 75% and 86%, respectively. Here, the typical electrochemical Pt features are still visible in the CV but in a lower intensity for catalyst Pt/gaSD_2100. The highest stability towards the ORR is observed for Pt/C ref (see Figures 6 and 7). Here, the mass activity decreases by 62%, while a loss of 42% is found for the $ECSA_{HUPD}$. In general, for implementation of such a sustainable material in a PEMFC, several improvements regarding the catalyst's morphology, intrinsic activity and knowledge about long-term behavior must be obtained. A sustainable catalyst support could be applied for both anode and cathode but other components of the PEMFC must be considered regarding their sustainability.

Furthermore, CO stripping experiments were performed before and after the AST to analyze changes of the nanoparticle's arrangement and tendency towards agglomeration. This

can be assumed by the formation of a CO oxidation peak at lower potentials originating from different potentials for CO oxidation on Pt surface and edges [45,46]. Figure 8 shows the CO stripping profiles of all four catalysts before and after the AST. In the initial state, all catalysts exhibit a CO oxidation peak around 0.80–0.85 V_{RHE} with different intensities corresponding to the available Pt surface area. All biochar-based catalysts show a small peak at lower potentials, indicating a certain fraction of agglomerated Pt nanoparticles in the pristine catalyst. This was not the case for a Black Pearl-based catalyst from our recent study, where the same Pt synthesis and deposition method was used [47]. Therefore, it can be assumed that Pt particles tend to agglomerate on the surface of the biochars to a certain degree.

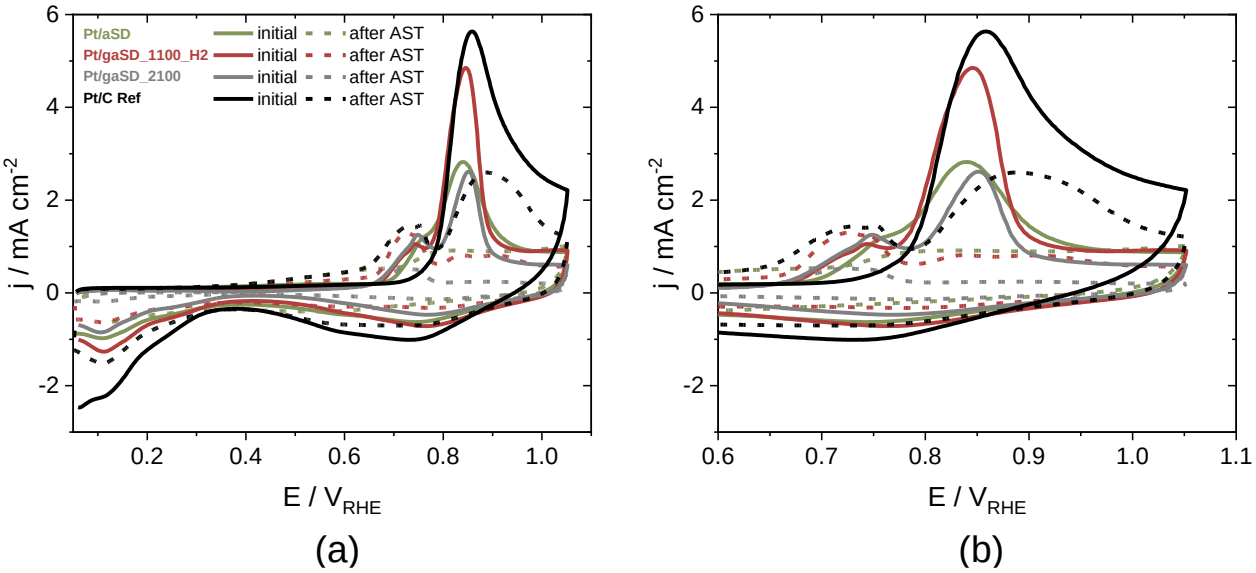

Figure 8. (**a**) Electrochemical CO stripping profile and (**b**) zoom of catalysts Pt/aSD, Pt/gaSD_1100_H2, Pt/gaSD_2100 and Pt/C ref before (initial) and after the AST (0.6–1.5 V_{RHE}, 5000 cycles) in CO−saturated electrolyte. Catalyst loading was 40 μg_{Pt} cm^{-2}.

After performing the AST, all samples reveal overall lower currents in the CO oxidation profiles. While Pt/gaSD_1100_H2 and Pt/C ref show the evolution of a dominant peak at lower potentials (Figure 8b), the overall CVs of Pt/aSD and Pt/gaSD_2100 basically show a flat shape without any distinct peaks. This matches the determined losses in $ECSA_{HUPD}$ where largely decreased values were observed for those two catalysts. For Pt/gaSD_1100_H2 it can be stated that the majority of the active Pt nanoparticles show a high ratio of rather agglomerated particles as the peak around 0.8 V_{RHE} almost totally diminishes. In case of Pt/C ref the dominating peak at higher potentials decreases and the peak at lower potentials arises, suggesting that the reduced $ECSA_{HUPD}$ after AST is at least partially caused by Pt particle agglomeration.

3. Materials and Methods

3.1. Modification of Sawdust

Steam activation followed by thermal treatment was used to modify the sawdust. The exact procedure is described in more detail below.

3.1.1. Activation of Biomass

In order to activate the untreated (pine) sawdust (ø = 0.05–0.1 µm, collected from Russia and provided by the Limited Liability Company SMNU Voskresenskoe as part of their collaboration with the IraSME project SUPERCONTCARBON), a steam activation was carried out. One (1) g of sawdust was inserted into a ceramic crucible and placed in a homemade vertical tube furnace. A round-bottom flask filled with deionized water was fixed at the bottom of the furnace and heated to 120 °C to ensure constant vapor production.

Afterwards, the furnace was heated to 750 °C and the temperature was held for 1 h under nitrogen/steam atmosphere. After 1 h, the furnace was cooled down and the obtained activated sawdust (aSD) was washed with 250 mL of deionized water and dried under air at 75 °C in an oven until the weight was constant.

3.1.2. High Temperature Treatment of Activated Biomass

The aSD was treated in a high-temperature furnace *LHTG 100-200-30* (Carbolite Gero, Neuhausen, Germany). 150 mg of aSD was put into a glassy carbon boat (HTW Hochtemperatur-Werkstoff, Thierhaupten, Germany) and was placed in the furnace chamber. After heating to 60 °C and maintaining vacuum for 30 min the high-temperature furnace was heated to the desired temperatures of 1500, 1800, 2100 or 2800 °C at a heating rate of 600 K h^{-1} (>2000 °C the heating rate was reduced to 500 K h^{-1}) under 200 L h^{-1} argon flow. After 1 h at the selected temperature, the furnace was cooled down to room temperature under nitrogen atmosphere. In addition, 150 mg of the aSD were thermally treated under H_2/Ar atmosphere (120 L h^{-1} H_2 and 120 L h^{-1} Ar resulting in 50 vol.% H_2) at 1100 °C. According to safety requirements when operating the furnace with H_2, it was necessary to purge the furnace with a flow rate of 3500 L h^{-1} N_2/Ar for at least 15 min before removing the samples.

3.2. Platinum Nanoparticle and Platinum Catalyst Synthesis

For platinum nanoparticle synthesis, a polyol route was used [39]. 725 mg chloroplatinic acid hexahydrate (1.4 mmol, 99.95%, Alfa Aesar, Kandel, Germany) and 80 mL ethylene glycol (≥99.5%, p.a., Rotipuran®, Carl Roth, Karlsruhe, Germany) were placed in a round flask. 12 mL of 2 mol L^{-1} NaOH in ethylene glycol was added to adjust a pH of 12. The solution was stirred for 4 h at 140 °C under reflux. Next, 19.53 mL of the resulting platinum nanoparticle suspension and ~40 mL of 1 mol L^{-1} HCl (p.a., VWR, Darmstadt, Germany) were centrifugated (Eppendorf, Hamburg, Germany) at 7000 rpm for 10 min. The supernatant was decanted and the process was repeated twice. The residue was dispersed in ~5 mL of acetone (p.a., Sigma Aldrich, Taufkirchen, Germany) and added to 60 mg of the carbon support. This suspension was sonicated until the acetone was evaporated. The platinum catalyst was washed with ultrapure water and dried at room temperature under vacuum.

3.3. Physical Characterization of Carbon Supports and Platinum Catalysts

For nitrogen sorption, about 100 mg of the samples were evacuated at 150 °C overnight and measured with *TriStar II 3020* (Micromeritics, Unterschleiβheim, Germany) in a relative pressure range 0.005 to 0.95. The free space was calculated by helium. To determine the specific surface area the Brunauer-Emmett-Teller (BET) formalism was used. The micropore volumes were calculated using carbon black reference of the t-plot method. Pore size distributions were determined using the non-local density functional theory (NLDFT) carbon model of MicroActive 3.0 software (Micromeritics, Unterschleiβheim, Germany).

For Raman spectroscopy and PXRD, ~1 mg of carbon materials were dispersed in 2-propanol (≥99.9%, Carl Roth, Germany), drop casted on a zero-background carrier and the solvent evaporated under air. Raman spectra were recorded with the confocal Raman microscope Senterra (Bruker, Leipzig, Germany) equipped with a He-Ne laser. To focus the sample, a light microscope BX51 (Olympus K.K., Tokyo, Japan) with an 20x magnification objective was used. A laser power of 2 mW, a wavelength of 633 nm, an averaging of 10 scans and resolution of 3–5 cm^{-1} were applied. The aperture was adjusted to 50 × 1000 µm and the measuring range was 50 to 3500 cm^{-1}. Three different positions per samples were measured and evaluated. To determine the $I_{D1/G}$ value, a fitting of the spectra was performed. A background correction was carried out with the software Unifit2020. For the first-order spectra four Lorentzian-shaped and one Gaussian-shaped peaks were fitted [32,37]. In detail, the G-, D1-, D2- and D4-bands are described by a Lorentzian curve shape and the D3-band followed the course of a Gaussian peak shape.

The peaks in the second-order spectrum were fitted with four Lorentzian shaped curves (G'-, D+G-, 2G- and 2D'-band), where the G'- and 2D'-band were very weakly pronounced and mostly only became clear as a shoulder of the D+G- and 2G-band [34,48,49].

PXRD measurements were performed using an Empyrean series 2 (PANalytical, Almelo, The Netherlands) in Bragg-Brentano-geometry. The copper anode of the X-ray source generates a K_α radiation with a wavelength of 0.154 nm. Samples were measured at 45 kV of acceleration voltage and a current of 40 mA in a 2θ range of 5 to 90°. The diffractograms were evaluated and compared to reference data base with the software HighScore Plus 4.1 (PANalytical, The Netherlands). The layer distance d(hkl) was obtained by BRAGG Equation (2). By this equation, the relationship between the d(hkl) and the angle θ(hkl) under irradiation of X-rays with the wavelength λ is described. This results in an ordering of the interference n:

$$2d_{hkl} \sin \theta_{hkl} = n\lambda \quad (2)$$

The crystallite size L_{hkl} is determined by the SCHERRER equation. First, the full width at half maximum (FWHM) of a reflex is determined. The crystallite size L(002) is calculated using the wavelength of the X-ray beam λ and the diffraction angle θ(002) according to Equation (3). In addition, a K-factor for the required crystal form is needed, which is assumed to be 0.94 [50] for graphene-like carbon [51]:

$$L_{002} = \frac{K\lambda}{FWHM \cos(\theta_{002})} \quad (3)$$

For transmission electron microscopy, the platinum catalysts (1 mg) were dispersed in 4 mL of ethanol (≥99.9%, Carl Roth, Germany). 5 µL of dispersion were drop casted to a polyvinyl formal-coated copper grid with 200 mesh and diameter of 3.05 mm (Plano, Wetzlar, Germany). The TEM images were taken with *EM900 N* (Carl Zeiss, Oberkochen, Germany) with 80 kV acceleration voltage and charge coupled device. For evaluation of the TEM images, the software ImageJ was used and 300 platinum nanoparticles were analyzed.

Quantitative Pt analysis for determination of catalyst loading was carried out with XSeries 2 (Thermo Fisher Scientific, Bremen, Germany) by ICP-MS. 2.0 mg of platinum catalyst was digested in 1.6 mL hydrochloric acid (35%, Rotipuran®, Supra, Carl Roth, Germany) and 1.2 mL nitric acid (69%, Rotipuran®, Supra, Carl Roth, Germany) for 17 h. The digestion was filtered, diluted to 250 mL and a further dilution by a factor of 5 was carried out. Calibration solutions (100, 200, 400, 600 and 800 µg L^{-1}) were prepared from a 1000 mg L^{-1} ICP platinum solution (Carl Roth, Germany). All measurement solutions contained 1 mg L^{-1} lutetium on basis of 1000 mg L^{-1} ICP lutetium solution (Carl Roth, Germany) as an internal standard.

3.4. Electrochemical Characterization

For electrochemical characterization a three electrode setup with a rotating disc electrode (RDE) as working electrode (WE), a reversible hydrogen electrode (RHE) as reference electrode (RE) and a platinum wire as counter electrode (CE) was used. The measurements were performed using 0.1 mol L^{-1} $HClO_4$ (p.a., Sigma Aldrich, Germany) electrolyte in a glass cell. The shaft of the RDE (Metrohm, Filderstadt, Germany) was made of polyetheretherketone (PEEK) and the disc electrode area was 0.1963 cm^2. A suspension of 6 mg platinum catalyst, 500 µL 2-Propanol and 1990 µL ultrapure water was prepared as catalyst ink. After 1 min in an ultrasonic bath, 20 µL of Nafion suspension (5 wt.% Nafion in aliphatic alcohol and water, Sigma Aldrich, Germany) was added and further sonicated for 15 min. The catalyst ink was homogenized with horn sonication (10% amplitude, 30 s pulse on, 30 s pulse off) for 4 min. In order to achieve an electrode loading of 40 μg_{Pt} cm^{-2}, 8.2 µL of the catalyst ink were coated on the electrode and dried at 60 °C for 3 min in an oven. For the electrochemical measurements a potentiostat of the type PGSTAT204 (Metrohm Autolab, Utrecht, The Netherlands) and the software NOVA 2.1 for data processing were used.

After N_2 saturation of the electrolyte for 20 min, 300 potential cycles in a range of 0.05–1.2 V_{RHE} with a scan rate of 500 mV s^{-1} were carried out for activation of the catalyst. Afterwards, three CVs from 0.05 to 1.05 V_{RHE} with a scan rate of 50 mV s^{-1} were recorded. The positive current range of the last cycle was chosen for evaluation of the ECSA from HUPD. The $ECSA_{HUPD}$ was evaluated in the positive current range (H^+ desorption).

The second method to analyze the ECSA was electrochemical CO stripping. For this method, CO was bubbled for 30 s through the electrolyte to cover the active Pt catalyst surface area. Subsequently, the remaining CO was removed by N_2 saturation of the electrolyte for 15 min. Afterwards, three CVs in the HUPD range (0.05–0.3 V_{RHE}) with a scan rate of 50 mV s^{-1} were performed to ensure complete CO poisoning on the platinum surface. Finally, the CO stripping was carried out by performing three cycles from 0.05 to 1.05 V_{RHE} with a scan rate of 50 mV s^{-1}.

Equation (4) was applied to calculate the ECSA under use of the scan rate v, the platinum charge L_{Pt} and the charge density C (210 µC $cm^{-2}{}_{Pt}$ [52] for a one electron transfer in case of protons and 420 µC $cm^{-2}{}_{Pt}$ [53] for a two electron transfer in case of CO).

$$ECSA = \frac{A_{Pt}}{v\ C\ L_{Pt}} \tag{4}$$

For determination of the ORR mass activity, CVs in O_2-saturated electrolyte were recorded at 1600 rpm in the range of 0.05–1.15 V_{RHE} with a scan rate of 5 mV s^{-1}. The current density j at a potential of 0.9 V_{RHE}, and the average of diffusion limited current density j_{lim} (0.1–0.5 V_{RHE}) was used to calculate the kinetic limited current density according to KOUTECKY-LEVICH in Equation (5). j and the catalyst mass on the electrode was used to determine the mass activity.

$$\frac{1}{j} = \frac{1}{j_{kin}} + \frac{1}{j_{lim}} \tag{5}$$

After the above-described electrochemical characterization an accelerated stress test (AST) by cycling the potential between 0.6 and 1.5 V_{RHE} at a scan rate of 500 mV s^{-1} in N_2-saturated electrolyte for 5000 cycles was carried out. Afterwards, the electrochemical characterization was repeated under the same conditions as described above. For each catalyst, two electrodes were coated from one catalyst ink. Both electrodes were electrochemically characterized and evaluated and averaged values are presented. Figure S1 in the Supplementary Material shows values for $ECSA_{HUPD}$ and mass activity of each measurement.

4. Conclusions

In this study, we investigated the effect of different activations for a waste biomass-based carbon as Pt catalyst support for the oxygen reduction reaction in acidic environment. Starting from steam-activated sawdust, different thermal treatment temperatures up to 2800 °C and furthermore reducing conditions were applied. The resulting carbon materials were intensively analyzed regarding changes in surface area and their graphitic nature using PXRD and Raman spectroscopy. It was found that a high treatment temperature leads to a highly graphitic material. A selection of carbons with significantly different material properties was chosen to be used as support to obtain a 40 wt.% Pt/C catalyst. Differences in metal loading on the support were claimed to depend on different surface properties of the carbons. Thermal treatment up to 2800 °C leads to a highly graphitized carbon but is however not sufficient for proper Pt nanoparticle deposition and distribution.

Electrochemical characterization towards the ORR resulted in lower activities for the aSD-based catalysts compared to a commercial reference. It was shown that solely graphitization at high temperatures does not lead to a strongly improved catalyst. However, the treatment in 50 vol.% H_2 atmosphere at moderate temperature of 1100 °C was found to increase the catalysts activity and stability. Losses in activity after the AST were assumed to stem from carbon corrosion as well as Pt nanoparticle deterioration. Furthermore, the activity and stability of the biochar-based catalysts was improved at high treatment temperatures but was still lower compared to the Pt/C reference. This was attributed to

differences in carbon aggregate size and tendency towards Pt agglomeration. Our study demonstrates that a high degree of graphitization alone in a biomass-based support for a Pt ORR catalyst is not sufficient to obtain a stable catalyst. The improvements observed from the influence of H_2 treatment reveal the potential of fabricating improved and sustainable catalysts. This includes furthermore optimization of activation procedure and for example a homogenization of carbon aggregates by ball milling.

Supplementary Materials: The following supporting information can be downloaded at: https://www.mdpi.com/article/10.3390/catal13020343/s1, Figure S1: Mass activities at 0.9 V_{RHE} (a) and $ECSA_{HUPD}$ (b) for catalysts Pt/aSD, Pt/gaSD_1100_H2, Pt/gaSD_2100 and Pt/C ref before (initial) and after the AST (0.6−1.5 V_{RHE}, 5,000 cycles). Results from two measurements are shown, indicated with 1 and 2.; Figure S2: Thermogravimetric profile of Pt/C ref in oxygen at a heating rate of 10 °C min^{-1} in the range of 30−900 °C with 40 mL min^{-1} O_2 flow. The remaining weight fraction of Pt is indicated.

Author Contributions: Conceptualization, N.B., H.S., O.A.I. and J.M.-H.; validation, N.B.; investigation, N.B. and J.M.-H.; data curation, N.B. and H.S.; writing—original draft preparation, H.S. and N.B.; writing—review and editing, H.S., N.B., J.M.-H., O.A.I., P.W. and M.W.; visualization, H.S. and N.B.; supervision, P.W. and M.W.; funding acquisition, P.W. All authors have read and agreed to the published version of the manuscript.

Funding: This research was funded by the Federal Ministry for Economic Affairs and Climate Action on the basis of a decision by the German Bundestag (grant number 03ETB016A). M.W. thanks the AiF-ZIM IraSME project "Supercontcarbon" (No. ZF4703301SA9) for financial support and O.A.I. acknowledges a scholarship (personal identification number: 91759017) by the German Academic Exchange Program (DAAD). The XRD instrument is funded by the German Science Foundation (DFG) through grant INST 184/154-1 FUGG.

Data Availability Statement: The data presented in this study are available on request from the corresponding author.

Acknowledgments: The authors acknowledge the Electron and Light Microcopy Service Unit at the Carl von Ossietzky University of Oldenburg for providing with the imaging facilities.

Conflicts of Interest: The authors declare no conflict of interest. The funders had no role in the design of the study; in the collection, analyses, or interpretation of data; in the writing of the manuscript, or in the decision to publish the results.

References

1. United Nations Framework Convention on Climate Change. *The Paris Agreement*; United Nations Framework Convention on Climate Change: Paris, France, 2015.
2. Shiva Kumar, S.; Himabindu, V. Hydrogen production by PEM water electrolysis—A review. *Mater. Sci. Energy Technol.* **2019**, *2*, 442–454. [CrossRef]
3. Li, Y.; Taghizadeh-Hesary, F. The economic feasibility of green hydrogen and fuel cell electric vehicles for road transport in China. *Energy Policy* **2022**, *160*, 1–43. [CrossRef]
4. Kreuer, K.-D.; Paddison, S.J.; Spohr, E.; Schuster, M. Transport in Proton Conductors for Fuel-Cell Applications: Simulations, Elementary Reactions, and Phenomenology. *Chem. Rev.* **2004**, *104*, 4637–4678. [CrossRef]
5. Rosli, R.E.; Sulong, A.B.; Daud, W.R.W.; Zulkifley, M.A.; Husaini, T.; Rosli, M.I.; Majlan, E.H.; Haque, M.A. A review of high-temperature proton exchange membrane fuel cell (HT-PEMFC) system. *Int. J. Hydrogen Energy* **2017**, *42*, 9293–9314. [CrossRef]
6. Bandlamudi, V.; Bujlo, P.; Sita, C.; Pasupathi, S. Study on electrode carbon corrosion of high temperature proton exchange membrane fuel cell. *Mater. Today Proc.* **2018**, *5*, 10602–10610. [CrossRef]
7. Holade, Y.; Morais, C.; Servat, K.; Napporn, T.W.; Kokoh, K.B. Enhancing the available specific surface area of carbon supports to boost the electroactivity of nanostructured Pt catalysts. *Phys. Chem. Chem. Phys.* **2014**, *16*, 25609–25620. [CrossRef]
8. Feng, L.; Sun, X.; Yao, S.; Liu, C.; Xing, W.; Zhang, J. Electrocatalysts and Catalyst Layers for Oxygen Reduction Reaction. In *Rotating Electrode Methods and Oxygen Reduction Electrocatalysts*; Elsevier: Amsterdam, The Netherlands, 2014; pp. 67–132.
9. Meier, J.C.; Galeano, C.; Katsounaros, I.; Witte, J.; Bongard, H.J.; Topalov, A.A.; Baldizzone, C.; Mezzavilla, S.; Schüth, F.; Mayrhofer, K.J.J. Design criteria for stable Pt/C fuel cell catalysts. *Beilstein J. Nanotechnol.* **2014**, *5*, 44–67. [CrossRef]
10. Wang, Z.-B.; Zuo, P.-J.; Chu, Y.-Y.; Shao, Y.-Y.; Yin, G.-P. Durability studies on performance degradation of Pt/C catalysts of proton exchange membrane fuel cell. *Int. J. Hydrogen Energy* **2009**, *34*, 4387–4394. [CrossRef]
11. Healy, J.; Hayden, C.; Xie, T.; Olson, K.; Waldo, R.; Brundage, M.; Gasteiger, H.; Abbott, J. Aspects of the Chemical Degradation of PFSA Ionomers used in PEM Fuel Cells. *Fuel Cells* **2005**, *5*, 302–308. [CrossRef]

12. Knights, S.D.; Colbow, K.M.; St-Pierre, J.; Wilkinson, D.P. Aging mechanisms and lifetime of PEFC and DMFC. *J. Power Sources* **2004**, *127*, 127–134. [CrossRef]
13. Wang, X.; Li, W.; Chen, Z.; Waje, M.; Yan, Y. Durability investigation of carbon nanotube as catalyst support for proton exchange membrane fuel cell. *J. Power Sources* **2006**, *158*, 154–159. [CrossRef]
14. Young, A.P.; Stumper, J.; Gyenge, E. Characterizing the Structural Degradation in a PEMFC Cathode Catalyst Layer: Carbon Corrosion. *J. Electrochem. Soc.* **2009**, *156*, B913–B922. [CrossRef]
15. Artyushkova, K.; Pylypenko, S.; Dowlapalli, M.; Atanassov, P. Structure-to-property relationships in fuel cell catalyst supports: Correlation of surface chemistry and morphology with oxidation resistance of carbon blacks. *J. Power Sources* **2012**, *214*, 303–313. [CrossRef]
16. Schmies, H.; Hornberger, E.; Anke, B.; Jurzinsky, T.; Nong, H.N.; Dionigi, F.; Kühl, S.; Drnec, J.; Lerch, M.; Cremers, C.; et al. Impact of Carbon Support Functionalization on the Electrochemical Stability of Pt Fuel Cell Catalysts. *Chem. Mater.* **2018**. [CrossRef]
17. Guo, L.; Jiang, W.J.; Zhang, Y.; Hu, J.S.; Wei, Z.D.; Wan, L.J. Embedding Pt Nanocrystals in N-Doped Porous Carbon/Carbon Nanotubes toward Highly Stable Electrocatalysts for the Oxygen Reduction Reaction. *ACS Catal* **2015**, *5*, 2903–2909. [CrossRef]
18. Tuaev, X.; Paraknowitsch, J.P.; Illgen, R.; Thomas, A.; Strasser, P. Nitrogen-doped coatings on carbon nanotubes and their stabilizing effect on Pt nanoparticles. *Phys. Chem. Chem. Phys.* **2012**, *14*, 6444–6447. [CrossRef]
19. Iwanow, M.; Gartner, T.; Sieber, V.; Konig, B. Activated carbon as catalyst support: Precursors, preparation, modification and characterization. *Beilstein J. Org. Chem.* **2020**, *16*, 1188–1202. [CrossRef]
20. Dhelipan, M.; Arunchander, A.; Sahu, A.; Kalpana, D. Activated carbon from orange peels as supercapacitor electrode and catalyst support for oxygen reduction reaction in proton exchange membrane fuel cell. *J. Saudi Chem. Soc.* **2017**, *21*, 487–494. [CrossRef]
21. Dhanasekaran, P.; Shukla, A.; Krishnan, K.N.; Rongrin, I.; Selvaganesh, S.V.; Kalpana, D.; Bhat, S.D. Enhancing stability and efficiency of oxygen reduction reaction in polymer electrolyte fuel cells with high surface area mesoporous carbon synthesized from spent mushroom compost. *Sustain. Energy Fuels* **2019**, *3*, 1012–1023. [CrossRef]
22. Schonvogel, D.; Nowotny, M.; Woriescheck, T.; Multhaupt, H.; Wagner, P.; Dyck, A.; Agert, C.; Wark, M. Hydrothermal Carbonization-Derived Carbon from Waste Biomass as Renewable Pt Support for Fuel Cell Applications: Role of Carbon Activation. *Energy Technol.* **2019**, *7*, 1900344. [CrossRef]
23. Thommes, M.; Kaneko, K.; Neimark, A.V.; Olivier, J.P.; Rodriguez-Reinoso, F.; Rouquerol, J.; Sing, K.S.W. Physisorption of gases, with special reference to the evaluation of surface area and pore size distribution (IUPAC Technical Report). *Pure Appl. Chem.* **2015**, *87*, 1051–1069. [CrossRef]
24. Sing, K.S.W. Reporting physisorption data for gas/solid systems with special reference to the determination of surface area and porosity (Recommendations 1984). *Pure Appl. Chem.* **1985**, *57*, 603–619. [CrossRef]
25. Rodriguez Correa, C.; Hehr, T.; Voglhuber-Slavinsky, A.; Rauscher, Y.; Kruse, A. Pyrolysis vs. hydrothermal carbonization: Understanding the effect of biomass structural components and inorganic compounds on the char properties. *Journal of Anal. Appl. Pyrolysis* **2019**, *140*, 137–147. [CrossRef]
26. Patrick, J.W. *Porosity in Carbons: Characterization and Applications*; Edward Arnold: London, UK, 1995; p. 331.
27. Dehkhoda, A.M.; Ellis, N.; Gyenge, E. Electrosorption on activated biochar: Effect of thermo-chemical activation treatment on the electric double layer capacitance. *J. Appl. Electrochem.* **2013**, *44*, 141–157. [CrossRef]
28. Manoj, B.; Kunjomana, A.G. Structural Characterization of Selected Indian Coals by X-ray Diffraction and Spectroscopic Techniques. *Trends Appl. Sci. Res.* **2012**, *7*, 434–444. [CrossRef]
29. Fromm, O.; Heckmann, A.; Rodehorst, U.C.; Frerichs, J.; Becker, D.; Winter, M.; Placke, T. Carbons from biomass precursors as anode materials for lithium ion batteries: New insights into carbonization and graphitization behavior and into their correlation to electrochemical performance. *Carbon* **2018**, *128*, 147–163. [CrossRef]
30. Debye, P.; Scherrer, P. Über die Konstruktion von Graphit und amorpher Kohle. *Nachr. Von Der Ges. Der Wiss. Zu Göttingen* **1917**, *1917*, 180–188.
31. Xia, S.; Cai, N.; Wu, J.; Xiao, H.; Hu, J.; Chen, X.; Chen, Y.; Yang, H.; Wang, X.; Chen, H. Synthesis and formation mechanism of biomass-based mesoporous graphitic carbon. *Fuel Process. Technol.* **2020**, *209*, 106543. [CrossRef]
32. Sadezky, A.; Muckenhuber, H.; Grothe, H.; Niessner, R.; Pöschl, U. Raman microspectroscopy of soot and related carbonaceous materials: Spectral analysis and structural information. *Carbon* **2005**, *43*, 1731–1742. [CrossRef]
33. Dresselhaus, M.S.; Jorio, A.; Hofmann, M.; Dresselhaus, G.; Saito, R. Perspectives on carbon nanotubes and graphene Raman spectroscopy. *Nano Lett.* **2010**, *10*, 751–758. [CrossRef]
34. Antunes, E.F.; Lobo, A.O.; Corat, E.J.; Trava-Airoldi, V.J.; Martin, A.A.; Veríssimo, C. Comparative study of first- and second-order Raman spectra of MWCNT at visible and infrared laser excitation. *Carbon* **2006**, *44*, 2202–2211. [CrossRef]
35. Rebelo, S.L.; Guedes, A.; Szefczyk, M.E.; Pereira, A.M.; Araujo, J.P.; Freire, C. Progress in the Raman spectra analysis of covalently functionalized multiwalled carbon nanotubes: Unraveling disorder in graphitic materials. *Phys. Chem. Chem. Phys.* **2016**, *18*, 12784–12796. [CrossRef]
36. Hulstede, J.; Schonvogel, D.; Schmies, H.; Wagner, P.; Schroter, F.; Dyck, A.; Wark, M. Relevant Properties of Carbon Support Materials in Successful Fe-N-C Synthesis for the Oxygen Reduction Reaction: Study of Carbon Blacks and Biomass-Based Carbons. *Materials* **2020**, *14*, 45. [CrossRef]

37. Ferrari, A.C.; Robertson, J. Interpretation of Raman spectra of disordered and amorphous carbon. *Phys. Rev. B* **2000**, *61*, 14095–14107. [CrossRef]
38. Zickler, G.A.; Smarsly, B.; Gierlinger, N.; Peterlik, H.; Paris, O. A reconsideration of the relationship between the crystallite size La of carbons determined by X-ray diffraction and Raman spectroscopy. *Carbon* **2006**, *44*, 3239–3246. [CrossRef]
39. Bock, C.; Paquet, C.; Couillard, M.; Botton, G.A.; MacDougall, B.R. Size-Selected Synthesis of PtRu Nano-Catalysts: Reaction and Size Control Mechanism. *J. Am. Chem. Soc.* **2004**, *126*, 8028–8037. [CrossRef] [PubMed]
40. Castanheira, L.; Silva, W.O.; Lima, F.H.B.; Crisci, A.; Dubau, L.; Maillard, F. Carbon Corrosion in Proton-Exchange Membrane Fuel Cells: Effect of the Carbon Structure, the Degradation Protocol, and the Gas Atmosphere. *ACS Catal* **2015**, *5*, 2184–2194. [CrossRef]
41. Shao, Y.; Zhang, S.; Kou, R.; Wang, X.; Wang, C.; Dai, S.; Viswanathan, V.; Liu, J.; Wang, Y.; Lin, Y. Noncovalently functionalized graphitic mesoporous carbon as a stable support of Pt nanoparticles for oxygen reduction. *J. Power Sources* **2010**, *195*, 1805–1811. [CrossRef]
42. Kameya, Y.; Hayashi, T.; Motosuke, M. Stability of platinum nanoparticles supported on surface-treated carbon black. *Appl. Catal. B Environ.* **2016**, *189*, 219–225. [CrossRef]
43. Kocha, S.S.; Shinozaki, K.; Zack, J.W.; Myers, D.J.; Kariuki, N.N.; Nowicki, T.; Stamenkovic, V.; Kang, Y.; Li, D.; Papageorgopoulos, D. Best Practices and Testing Protocols for Benchmarking ORR Activities of Fuel Cell Electrocatalysts Using Rotating Disk Electrode. *Electrocatalysis* **2017**, *8*, 366–374. [CrossRef]
44. Kongkanand, A.; Mathias, M.F. The Priority and Challenge of High-Power Performance of Low-Platinum Proton-Exchange Membrane Fuel Cells. *J. Phys. Chem. Lett.* **2016**, *7*, 1127–1137. [CrossRef]
45. Guerin, S.; Hayden, B.E.; Lee, C.E.; Mormiche, C.; Owen, J.R.; Russell, A.E.; Theobald, B.; Thompsett, D. Combinatorial electrochemical screening of fuel cell electrocatalysts. *J. Comb. Chem.* **2004**, *6*, 149–158. [CrossRef]
46. Maillard, F.; Eikerling, M.; Cherstiouk, O.V.; Schreier, S.; Savinova, E.; Stimming, U. Size effects on reactivity of Pt nanoparticles in CO monolayer oxidation: The role of surface mobility. *Faraday Discuss* **2004**, *125*, 357–377. [CrossRef]
47. Müller-Hülstede, J.; Nagappan, N.K.; Bengen, N.; Uhlig, L.M.; Schonvogel, D.; Wagner, P. Comparative Study of Platinum Nanoparticle Deposition on TiO2/BP and SnO2/BP Nanocomposites for the Oxygen Reduction Reaction. *ECS Trans.* **2022**, *109*, 425. [CrossRef]
48. Vollebregt, S.; Ishihara, R.; Tichelaar, F.D.; Hou, Y.; Beenakker, C.I.M. Influence of the growth temperature on the first and second-order Raman band ratios and widths of carbon nanotubes and fibers. *Carbon* **2012**, *50*, 3542–3554. [CrossRef]
49. Bokobza, L.; Zhang, J. Raman spectroscopic characterization of multiwall carbon nanotubes and of composites. *eXPRESS Polym. Lett.* **2012**, *6*, 601–608. [CrossRef]
50. Saikia, B.; Boruah, R.; Gogoi, P. A X-ray diffraction analysis on graphene layers of Assam coal. *J. Chem. Sci.* **2009**, *121*, 103–106. [CrossRef]
51. Waseda, Y.; Matsubara, E.; Shinoda, K. *X-Ray Diffraction Crystallography*; Springer: Berlin, Germany, 2011.
52. Li, W.; Lane, A.M. Resolving the HUPD and HOPD by DEMS to determine the ECSA of Pt electrodes in PEM fuel cells. *Electrochem. Commun.* **2011**, *13*, 913–916. [CrossRef]
53. Rudi, S.; Cui, C.; Gan, L.; Strasser, P. Comparative Study of the Electrocatalytically Active Surface Areas (ECSAs) of Pt Alloy Nanoparticles Evaluated by Hupd and CO-stripping voltammetry. *Electrocatalysis* **2014**, *5*, 408–418. [CrossRef]